Catalysis Science & Technology

ROYAL SOCIETY OF CHEMISTRY

PAPER

View Article Online
View Journal | View Issue

Cite this: *Catal. Sci. Technol.*, 2023, **13**, 1111

Mechanistic insight into low temperature SCR by ceria–manganese mixed oxides incorporated into zeolites†

Nicholas C. Nelson, [a] Tahrizi Andana,[a] Kenneth G. Rappé *[a] and Yong Wang [ab]

Recent efforts to increase the low-temperature activity of zeolite-based selective catalytic reduction (SCR) catalysts has led to the exploration of hybrid materials comprised of a metal oxide and zeolite phase. However, the role of each component in promoting low temperature activity and their interaction with each other is not well understood. Herein, we attempt to understand the low temperature promotion by synthesizing a series of ceria–manganese mixed oxides introduced to a H-SSZ-13 zeolite *via* incipient wetness impregnation of the oxide precursors. Our data suggests that the mixed oxide phase provides access to surface fast SCR reaction channels *via* SCR generation of adsorbed nitrogen dioxide and its derivatives. At low temperature (100–170 °C), where the SCR promotion is greatest, we show that it is unfavorable for the adsorbed nitrogen dioxide (derivatives) to react with ammonia to form ammonium nitrate. This implies that fast SCR pathways remain accessible on the oxide at low temperatures and are not blocked by ammonium nitrate deposits as they are on the pure zeolite component. We hypothesize that this a contributing factor for the observed low temperature SCR promotion. Our results may benefit the current understanding of hybrid SCO–SCR catalysts and lead to further technological development in this area.

Received 8th November 2022,
Accepted 6th January 2023

DOI: 10.1039/d2cy01921c

rsc.li/catalysis

Introduction

Ammonia selective catalytic reduction (NH_3-SCR) over zeolite-based materials has seen expansive industrial adoption for the abatement of pollutants in diesel engines.[1] A perennial challenge in these SCR devices is to maintain (near) stoichiometric conversion of criterion pollutants at ever decreasing temperatures. One strategy to meet this challenge leverages the faster SCR kinetics afforded by increasing the nitrogen dioxide (NO_2) to nitric oxide (NO) ratio at the SCR inlet to the point of unity, NO_2/NO_x = 0.5.[2] This strategy has been commercially implemented by introducing an oxidation catalyst (*e.g.*, a DOC) upstream of the SCR device. The DOC increases the NO_2/NO_x ratio at the SCR inlet through NO oxidation; however, the benefits of this strategy on state-of-the-art zeolite-based systems are limited to temperatures above *ca.* 200 °C. This temperature limitation arises due to the sluggish NO oxidation kinetics of the DOC and reversible fouling of zeolite-based SCR catalysts caused by the association of adsorbed NO_2 and NH_3 to form ammonium nitrate (NH_4NO_3) deposits.[2–4]

A nascent technology to alleviate the pitfalls associated with the DOC-SCR coupled system incorporates a selective catalytic oxidation (SCO) functionality directly onto the SCR catalyst.[5] This SCR composite catalyst system mitigates the sluggish NO oxidation kinetics of the DOC by nullifying the energetically demanding desorption of NO_2 and mitigates the effects of NO_2 reduction by CO and hydrocarbons in the DOC, *i.e.* increases efficiency.[4,5] These SCR composite catalysts are typically comprised of a Cu- or Fe-zeolite combined with a metal oxide phase that is introduced *via* a metal salt solution or mechanical mixing of the zeolite and preformed oxide.[5] It is well established that the efficacy of these hybrid systems depend on the ability of the zeolite and oxide components to transfer reactive species to one another through surface diffusion as opposed to in the gas phase.[6–9] However, the atomistic details have not yet been clarified owing to the complex nature of SCR chemistry and the equally complex nature of the composite catalysts.[10]

As alluded to above, the zeolite and oxide components are not additive in the sense that the oxide component catalyzes NO oxidation to provide the zeolite access to fast SCR channels.[8,10] Nonetheless, the NO oxidation activity of the oxide typically runs parallel to the low temperature SCR

[a] *Energy & Environment Directorate, Pacific Northwest National Laboratory, Richland, WA 99354, USA. E-mail: ken.rappe@pnnl.gov*
[b] *The Gene and Linda Voiland School of Chemical Engineering and Bioengineering, Washington State University, Pullman, WA, USA*

† Electronic supplementary information (ESI) available: Catalytic activity, infrared spectra, temperature programmed experiments. See DOI: **https://doi.org/10.1039/d2cy01921c**

promotion observed in the composite systems.[6,10] This suggests that adsorbed NO_2 and/or its derivatives (*e.g.* HNO_2) are key intermediates that give rise to the low temperature promotion. Moreover, the oxidation of NO to NO_2, or the formation of the active site that leads to NO oxidation, is widely regarded to be kinetically relevant under standard SCR conditions (NO_2/NO_x = 0) over commercial zeolite-based catalysts.[11,12] Considering these observations, it may be prudent to view the SCR composite system through the lens of NO_2-SCR (eqn (1)).

$$2NO_2 + 2NH_3 = N_2 + NH_4NO_3 + H_2O \quad (1)$$

Iwasaki and Shinjoh compared SCR reactions spanning NO_2/NO_x ratios from zero to one over Fe/ZSM-5.[13] They found that below 175 °C, fast SCR (NO_2/NO_x = 0.5) activity dropped precipitously while the apparent activity of NO_2-SCR increased as the temperature decreased. They attributed the negative temperature coefficient of NO_2-SCR to the formation of solid NH_4NO_3 *via* eqn (1). Previous studies by Koebel *et al.*[2] and subsequent *in situ* IR studies confirmed the formation of NH_4NO_3 on zeolite-based materials during low temperature NO_2-SCR.[14] These studies demonstrated that NO_2-SCR represents a low energy pathway towards NO_x abatement that is thermodynamically driven by NH_4NO_3 precipitation. However, as aforementioned, NH_4NO_3 accumulation results in reversible catalyst fouling. These observations suggest that identifying materials that catalyze both NO oxidation to NO_2 and NH_4NO_3 decomposition at low temperature (<175 °C) would promote standard SCR. Indeed, Tronconi *et al.*[15] demonstrated a remarkable intermediate temperature (>175 °C) SCR promotion over Fe/ZSM-5 by replacing O_2 (in the case of standard SCR) or NO_2 (in the case of fast SCR) with NH_4NO_3 (eqn (2)).

$$2NH_3 + 2NO + NH_4NO_3 = 3N_2 + 5H_2O \quad (2)$$

Here, NH_4NO_3 can simply be regarded as a masked NO_2 molecule and negates the need for the kinetically relevant oxidation of NO by O_2 under standard SCR conditions.[11] Ensuing work by Tronconi *et al.*[16] proved this by demonstrating the equivalence of NO_2 and NH_4NO_3 through comparison of their respective SCR rates, both of which were far beyond those of standard SCR.

Our aim in this study was to identify potential contributing factors that lead to low temperature SCR promotion in SCR composite catalyst systems. To this end, we synthesized a series of hybrid materials by introducing ceria–manganese mixed oxides to H-SSZ-13 zeolite *via* incipient wetness impregnation of the oxide precursors. Ceria–manganese mixed oxides were chosen owing to their activity for NO oxidation.[17] Our data suggests that the role of the ceria–manganese mixed oxide phase is to generate NO_2 and its derivatives through NO oxidation. This provides the hybrid material access to surface fast SCR reaction channels that are not readily accessible during standard SCR over commercial Cu-based chabazite materials. However, the oxidation activity of the mixed oxide is not restricted to NO. The low oxidation selectivity results in parasitic NH_3 oxidation and limits the SCR activity over the oxide component at and above intermediate temperatures (*ca.* >170 °C). An apparent role of the zeolite then is to provide a reservoir of accessible NH_3 reductant to the oxide phase. In addition to this, the oxide component circumvents NH_4NO_3 fouling by disfavoring its formation. It is possible that this and the NO oxidation activity are key contributing factors for low temperature promotion over the oxide.

Experimental

Reagents

Cerium(III) nitrate hexahydrate ($Ce(NO_3)_3{\cdot}6H_2O$) was purchased from Alfa Aesar. Trimethyladamantylammonium hydroxide (TMAda-OH, ~25 wt%) was purchased from Sachem Inc. Manganese(II) nitrate hydrate ($Mn(NO_3)_2{\cdot}xH_2O$), Aluminum(III) hydroxide ($Al(OH)_3$), LUDOX AS-30, Davisil grade 645, pore size 150 Å, 60–100 mesh (SiO_2), sodium hydroxide (NaOH),and ammonium nitrate (NH_4NO_3) were purchased from Sigma Aldrich. For $Mn(NO_3)_2{\cdot}xH_2O$, x was assumed equal to zero for calculation purposes.

Synthesis

H-SSZ-13. The zeolite support was prepared by adding 1.5 g of $Al(OH)_3$ into stirring (400 rpm) 0.2 M NaOH aqueous solution at room temperature. Then, 17 g of TMAda-OH solution was added into the mixture. After 1 h under continuous stirring, 40 g of LUDOX AS-30 was poured slowly into the mixture. After 2 h under continuous stirring, the precursor gel with the following molar composition (SDA : $NaOH : SiO_2 : Al_2O_3 : H_2O$ = 10 : 10 : 98 : 4 : 2200) was obtained and transferred into a 125 ml Teflon-lined stainless-steel autoclave equipped with magnetic stirrer. The hydrothermal synthesis then proceeded with heating the autoclave in a sand bath at 160 °C for 96 h under continuous stirring (300 rpm). After the synthesis, the white solid was recovered *via* centrifugation and rinsed with deionized water. This process was repeated three times. The solid was then dried overnight under the flow of N_2 at 70 °C and finally calcined in a muffle furnace at 550 °C for 4 h. The parent zeolite was then transformed into the NH_4-form (NH_4^+-SSZ-13) *via* two-time ion-exchange with NH_4NO_3 aqueous solution (weight ratio of Na-SSZ-13 : NH_4NO_3 : H_2O = 5 : 4 : 50) carried out at 80 °C for 2 h. The solid was recovered *via* centrifugation and rinsed with deionized water after each exchange. This recovery process was repeated three times. Finally, the material was calcined in air at 550 °C for 6 h with a 2 °C min^{-1} heating rate. The Si/Al ratio of 11.8 has been confirmed *via* ICP-AES.

$Ce_xMn_{1-x}O_y$. Ceria (CeO_2) was synthesized through calcination of $Ce(NO_3)_3{\cdot}6H_2O$ in air at 650 °C for 5 h with a 2 °C min^{-1} heating rate. Ceria–manganese mixed oxide ($Ce_{0.7}Mn_{0.3}O_y$) was prepared by dissolving $Ce(NO_3)_3{\cdot}6H_2O$ (3.49 g, 8.04 mmol) and $Mn(NO_3)_2{\cdot}xH_2O$ (0.611 g, 3.41 mmol) in 6

mL of water. The water was removed by evaporation at 80 °C for 2 h. The dried mixed salt were heated to 650 °C for 5 h with a 2 °C min^{-1} heating rate. The other ceria–manganese mixed oxide ($Ce_{0.5}Mn_{0.5}O_y$) was prepared in the same way, but using $Ce(NO_3)_3{\cdot}6H_2O$ (1.08 g, 2.50 mmol) and $Mn(NO_3)_2{\cdot}xH_2O$ (0.438 g, 1.80 mmol).

$Ce_xMn_{1-x}O_y$/H-SSZ-13. The nominal weight loading for all zeolite-supported oxides was 25 wt%. For x = 1, $Ce(NO_3)_3{\cdot}6H_2O$ (0.1529 g, 0.352 mmol) was dissolved in 75 μL of deionized water. The solution was impregnated onto the H-SSZ-13 zeolite (0.237 g, ~0.3 mL g^{-1} pore volume) and mixed thoroughly with a mortar and pestle. For x = 0.7, $Ce(NO_3)_3{\cdot}6H_2O$ (0.1323 g, 0.305 mmol) and $Mn(NO_3)_3{\cdot}xH_2O$ (0.0233 g, 0.130 mmol) were dissolved in 75 μL of deionized water. The solution was impregnated onto the H-SSZ-13 zeolite (0.258 g, ~0.3 mL g^{-1} pore volume) and mixed thoroughly with a mortar and pestle. For x = 0.5, $Ce(NO_3)_3{\cdot}6H_2O$ (0.1078 g, 0.248 mmol) and $Mn(NO_3)_3{\cdot}xH_2O$ (0.0437 g, 0.244 mmol) were dissolved in 75 μL of deionized water. The solution was impregnated onto the H-SSZ-13 zeolite (0.256 g, ~0.3 mL g^{-1} pore volume) and mixed thoroughly with a mortar and pestle. All materials were subsequently calcined in air at 600 °C for 6 h with a 2 °C min^{-1} heating rate.

Activity testing

All the catalytic tests were carried out in a fixed-bed reactor comprised of a vertically mounted quartz tube (12.7 mm OD) with a K-type thermocouple placed upstream of the catalytic bed, a PID-controlled tubular furnace, a MKS MultiGas™ 2030 FTIR Continuous Gas Analyzer, and a set of Brooks 5850E Series mass flow controller and Brooks 0254 Series control box. Typically, 25 mg of catalyst (60–80 mesh) and 150 mg of SiO_2 (60–100 mesh) were homogeneously mixed and loaded into the reactor. The total reactant flow rate was set at 1.5 L min^{-1} (space velocity = 4.6×10^6 h^{-1} for bulk $Ce_xMn_{1-x}O_y$ and 1.7×10^6 h^{-1} for $Ce_xMn_{1-x}O_y$/H-SSZ-13), and both NO oxidation and standard SCR tests were conducted with a heating rate of 10 °C min^{-1}. For NO oxidation, the feed was comprised of 330 ppm NO and 15% O_2. For standard SCR, the feed was comprised of 330 ppm NO, 330 ppm NH_3, and 15% O_2. The NO_2 yield is defined below. All temperature programmed decomposition and reactions with NH_4NO_3 were carried out using the same setup. In a typical experiment, 18 μL of an NH_4NO_3 aqueous stock solution (0.492 mg μL^{-1}) was impregnated onto ~60 mg of catalyst. The material was dried in air at room temperature for >24 h prior to temperature programmed experiment.

$$NO_2\ \text{Yield} = 100 \times \frac{NO_{2,out} - NO_{2,in}}{NO_{in} + NO_{2,in}}$$

$$NO_x\ \text{Conversion} = 100*$$

$$\frac{(NO + NO_2 + NH_3)_{in} - (NO + NO_2 + NH_3)_{out}}{(NO + NO_2 + NH_3)_{in}}$$

$$N_2\ \text{Yield} = 100*$$

$$\frac{(NO + NO_2 + 2N_2O + NH_3)_{in} - (NO + NO_2 + 2N_2O + NH_3)_{out}}{(NO + NO_2 + 2N_2O + NH_3)_{in}}$$

Diffuse Reflectance Infrared Fourier Transform Spectroscopy

In situ DRIFTS analysis was performed on a Nicolet iS50R FTIR spectrometer equipped with an MCT/A detector and Harrick Praying Mantis™ high temperature reaction chamber (HVC-DRM-5) with ZnSe windows. Spectra were recorded with a mirror velocity of 1.8988 cm s^{-1}, aperture setting of 32, spectral resolution of 4 cm^{-1} with zero-filling of two, and 16 scans per spectrum. Where applicable, the spectra were recorded with a time interval of 10 seconds and are reported in Kubelka-Munk (K-M) units. The gases were delivered to the reaction chamber using a gas manifold equipped with electronic mass flow controllers and two-position-four-port switching valves. Background spectra were collected under He flow at 150 °C. Prior to background acquisition the sample was pretreated to 500 °C under 2% O_2/He and held for 15 min, followed by a 45 min purge under He flow at 500 °C. In a typical experiment, the gas feed composition was 330 ppm NO, 330 ppm NH_3, and/or 2% O_2 with a total flow rate of 100 mL min^{-1} (balanced by He) vented to atmosphere. Following each test, surface species were removed by repeating the pretreatment procedure.

Characterization

Textural properties. Surface area and pore structure of the samples were analysed by N_2 adsorption at 77 K with an automatic gas sorption system: Quadrasorb EVO/SI from Quantachrome Instruments. The samples were degassed under vacuum at 150 °C for 12 h before the adsorption measurement. The surface area was determined using 5 points BET (Brunauer–Emmett–Teller) method. The BJH (Barrett–Joyner–Halenda) method was used for the pore volume determination. Micropore surface was determined using the *t*-plot method. The results can be found in Table S1 of the ESI.†

X-Ray diffraction. Powder X-ray diffraction patterns were collected from powders packed into zero-background well holders using a Rigaku SmartLab SE diffractometer. The instrument employed Bragg–Brentano geometry with a Cu X-ray source (λ = 1.5418 Å), a variable divergence slit, and a high-speed D/teX Ultra 250 1D detector. Patterns were collected between 2 and 100° 2θ at intervals of 0.01° 2θ. The patterns can be found in Fig. S1 of the ESI.†

Results and discussion

Our group recently studied the promotional role of a cerium-manganese mixed oxide phase incorporated into a Cu-SSZ-13 catalyst for low-temperature ammonia SCR activity.[9] The promotional effect of the mixed oxide phase on SCR

performance observed in that work depended on the proximity between the Cu zeolite and oxide phases. Incipient wetness impregnation of the mixed oxide onto the Cu-SSZ-13 and ball milling of the preformed mixed oxide and zeolite resulted in greater SCR promotion relative to simple physical mixing of the preformed mixed oxide and zeolite catalyst particles. Additionally, there were further differences in the impregnated and ball milled samples such as susceptibility of NH_3 to non-selective (*i.e.*, parasitic) oxidation. Here, we aim to better understand the promotional role of the oxide phase.

We prepared a series of catalysts that are analogous to the $Ce_xMn_{1-x}O_y$/Cu-SSZ-13 composite catalyst system. We omitted Cu from our catalyst system to enable a focused study on the role of the mixed oxide phase. This is justified on the basis that the activity of the $Ce_xMn_{1-x}O_y$/Cu-SSZ-13 composite catalyst was the sum of the individual activity of the Cu-SSZ-13 and $Ce_xMn_{1-x}O_y$/H-SSZ-13 phases in the low-to-intermediate temperature (<200 °C) regime; thus, the observed activity promotion observed in this regime resulted from the interaction of the mixed oxide and H-SSZ-13.[9] Catalysts were prepared through incipient wetness impregnation of H-SSZ-13 with cerium and manganese nitrate salts with a nominal mixed oxide composition of Ce_x-$Mn_{1-x}O_y$/H-SSZ-13 where x = 1, 0.7, 0.5.

The impetus for incorporating the mixed oxide phase was to provide an NO oxidation functionality to Cu-SSZ-13. Our hypothesis was that the NO oxidation functionality could enable fast SCR reaction pathways (NO_2/NO_x = 0.5) under a standard SCR gas feed (NO_2/NO_x = 0). To test this hypothesis, we measured the NO oxidation activity across the three composite catalysts. Fig. 1a shows that increasing the amount of Mn in the oxide phase of the composite catalyst resulted in an increase in the NO_2 yield. The same trend was observed for the NO_x conversion (Fig. 1c) and the N_2 yield (Fig. S2†) during SCR over the composite catalyst.

A primary role of the zeolite phase in ammonia SCR is to provide a Bronsted acid site that stores NH_3. Our previous work showed that NH_3 storage at the Bronsted acid site was critical for the mixed oxide to promote low-temperature SCR in the composite catalyst.[9] Considering this, we carried out NO oxidation activity experiments on the composite catalysts in the presence of pre-adsorbed NH_3 to determine how zeolite-stored ammonia effects the NO_2 yield. For this experiment, NO oxidation measurements were preceded by introducing 330 ppm NH_3 to the NO oxidation feed (*i.e.*, NO + O_2 + NH_3) at 100 °C for 30 min followed by purging for 10 min with the NO oxidation feed (*i.e.*, NO + O_2). The trend of NO oxidation activity amongst the composite catalysts remained unchanged as shown in Fig. 1b. However, there were distinct differences between the activity profiles in Fig. 1a and b. The most notable difference was curvature change of the NO oxidation light-off profiles following NH_3 exposure. The curvature changes for CeO_2, $Ce_{0.7}Mn_{0.3}O_y$, and $Ce_{0.5}Mn_{0.5}O_y$ occurred around 270 °C, 200 °C, and 170 °C, respectively, and coincided with a slight increase in the NO

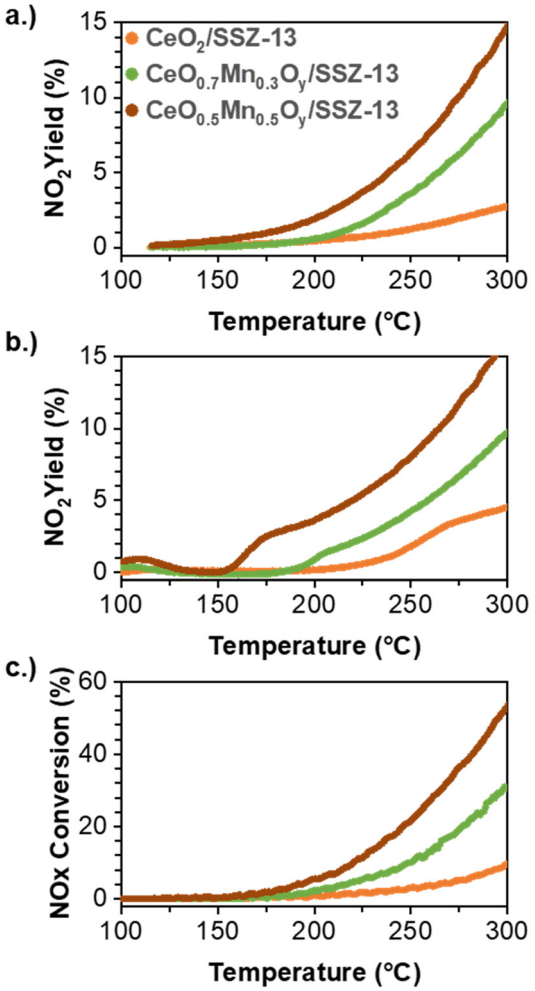

Fig. 1 NO oxidation activity over $Ce_xMn_{1-x}O_y$/H-SSZ-13 (a) without and (b) with pre-adsorbed NH_3. Reaction conditions: [NO] = 325 ppm; [NO_2] = 6 ppm; [O_2] = 15%; [N_2] = balance; flow rate = 1.5 SLM; GHSV = 1.7e + 6 h^{-1}. c.) SCR activity over $Ce_xMn_{1-x}O_y$/H-SSZ-13. Reaction conditions: same as (a and b) but with [NH_3] = 330 ppm.

concentration measured at the reactor outlet (Fig. S3†). In other words, the NO_2 evolution that caused the change in curvature was not derived exclusively from oxidation of the NO inlet feed in that moment. This observation suggests that, in the presence of pre-adsorbed NH_3, a metastable intermediate was formed under NO oxidation conditions and that at least one of the decomposition products was NO_2. The decomposition temperature of this intermediate in our test profile depended on the catalyst composition as evidenced from Fig. 1b. This implies that the intermediate was either formed on or diffused to the oxide phase prior to decomposition. In the absence of zeolite, *i.e.*, over the bulk mixed oxide, no curvature change was observed under an identical gas feed protocol (Fig. S4†). This demonstrates the requirement for stored ammonia in the zeolite to affect the curvature changes observed in Fig. 1. It is important to note that the rate of NO_2 formation from the metastable intermediate exceeded the rate of NO_2 formation from NO oxidation, which was the reason for the curvature change.

Diffuse Reflectance Infrared Fourier Transform Spectroscopy (DRIFTS) was utilized to elucidate the species formed upon co-adsorption of NO, O_2, and NH_3. We began our study with the bulk mixed metal oxide to delineate species adsorbed on the mixed oxide phase and the zeolite phase. Adsorption of NO onto $Ce_{0.7}Mn_{0.3}O_x$ at 150 °C (Fig. S5-a†) resulted in the formation of nitrite (1163 cm^{-1}) and hyponitrite (1102 cm^{-1}) species along with several lower intensity bands spanning from 1200 cm^{-1} to 1600 cm^{-1}. The bands in the latter region are attributed to nitrate and its derivatives (*e.g.*, N_2O_3).[18,19] The latter assignment was supported by the time-dependent evolution of these bands upon co-adsorption of NO and O_2 (Fig. S5-b†).

After the co-adsorption of NO and O_2, we purged the DRIFTS cell with He and then admitted a feed of 330 ppm NH_3 in He. The dynamic evolution of NO_2-derived species during the experiment is shown in Fig. 2a. The detailed changes that occurred are beyond the scope of this manuscript, but general relevant observations are addressed. From the DRIFTS experiment, it can be concluded that adsorbed NO_2 and/or its derivatives are perturbed upon exposure to NH_3. This was especially noticeable within the 1600–1400 cm^{-1} region which is commonly associated with monodentate and bidentate nitrates.[18] The perturbation can be interpreted as an interaction or association between NH_3 and NO_2-derived species. The nature of the perturbation was likely chemical, as opposed to physical, owing to the negative order of NH_3 on NO_2 yield during NO oxidation (Fig. 2b). The inhibition of gaseous NH_3 on NO_2 yield was caused by the relatively favorable SCR kinetics (Fig. S2†).

The interaction between NH_3 and NO_2 co-adsorbates discussed above points toward a nitroamine (NH_xNO_y) intermediate that may have given rise to the low-temperature NO_2 evolution shown in Fig. 1b. Although the exact form of this nitroamine complex remains unknown, we reasoned that its reactivity on the different oxide catalysts should scale proportionally with the reactivity of ammonia nitrate, NH_4NO_3. To assess this, we used NH_4NO_3 as a surrogate to the true nitroamine complex to gain a better understanding of how nitroamine complexes react over the mixed oxide component. The reactivity and product selectivity of NH_4NO_3 decomposition over the zeolite (in the absence of oxide) and the bulk oxide (in the absence of zeolite phase) were tested through impregnation of aqueous NH_4NO_3 followed by a temperature ramp under N_2 (Fig. S6†). The plot in Fig. 3a shows that the main NH_4NO_3 decomposition product over the zeolite was N_2O. The formation of N_2O was a direct or primary decomposition product (eqn (3)) and is the expected product from the thermal decomposition of NH_4NO_3.

$$NH_4NO_3 = N_2O + 2H_2O \quad (3)$$

In contrast, the main decomposition product was NO_2 across the oxide catalysts and represented *ca.* 75% of the total desorption products observed (Fig. 3a). The evolution of NO_2 from NH_4NO_3 decomposition over the oxide catalysts

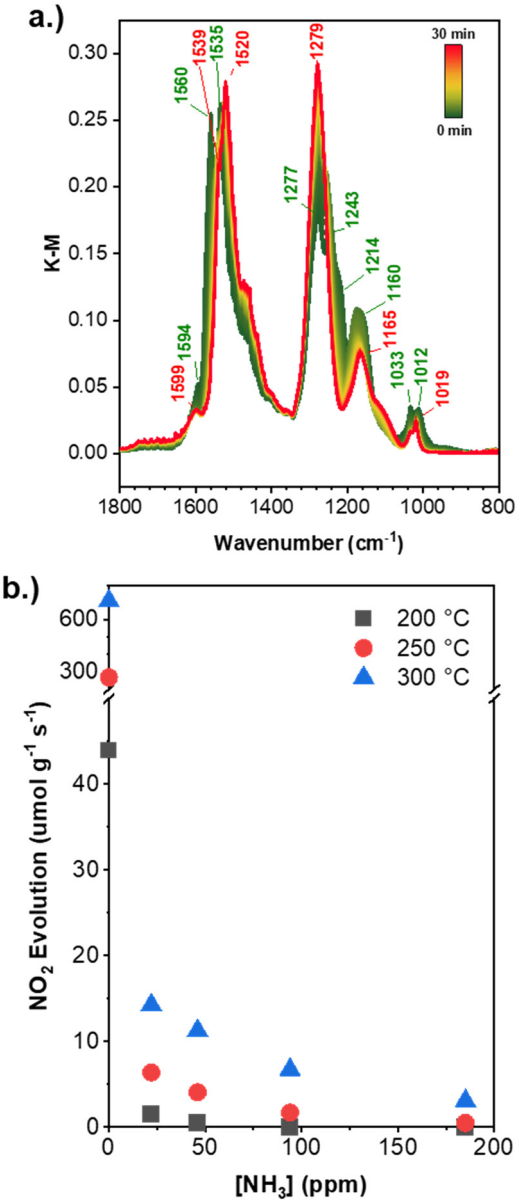

Fig. 2 a.) DRIFTS spectra recorded over bulk $Ce_{0.7}Mn_{0.3}O_y$ under NH_3 feed following pre-exposure to NO + O_2 gas feed. A He purge was interjected between the NH_3 and NO + O_2 gas feed. b.) NO oxidation activity as a function of NH_3 concentration and temperature over bulk $Ce_{0.7}Mn_{0.3}O_y$. Reaction conditions: [NO] = 325 ppm; [NO_2] = 6 ppm; [O_2] = 15%; [N_2] = balance; flow rate = 1.5 SLM; GHSV = 4.6e + 6 h^{-1}.

indicated that secondary reactions occurred. The secondary pathways are seemingly related to oxidation of NH_3 in NH_4NO_3. This is supported by the higher average oxidation state of nitrogen-containing species evolved over the oxide (*ca.* +2.5) relative to the zeolite (−1.0). The difference in average oxidation states was primarily caused by the larger amount of NO_2 evolved over the oxides at the expense of evolved NH_3 and N_2O. Further support for NH_3 oxidation over bulk $Ce_{0.7}Mn_{0.3}O_x$ came from the NH_3 temperature programmed reaction (TPR), desorption (TPD), and NH_3 adsorption DRIFTS analyses (Fig. S7†). The NH_3 TPR profile showed the

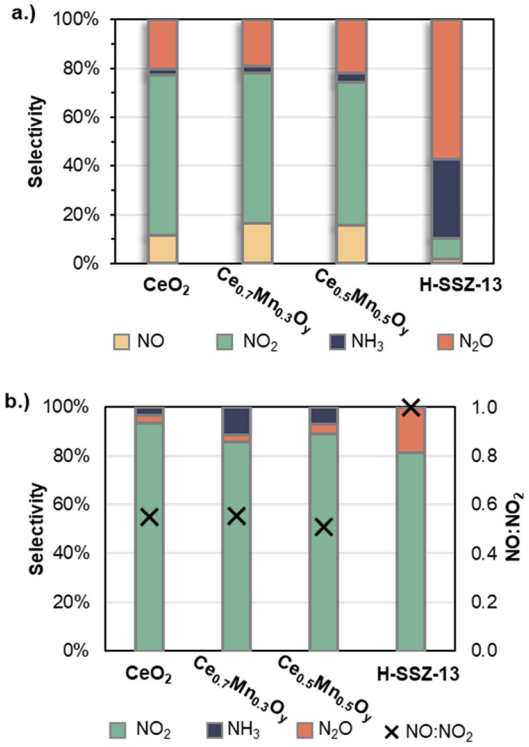

Fig. 3 Observed product distribution over various catalysts upon impregnation with aqueous NH_4NO_3 followed by heating under (a) N_2 and (b) NO. The right *y*-axis in (b) represents the ratio of NO consumed to the amount of NO_2 produced. Conditions: [NH_4NO_3] = 15 wt%; [NO] = 325 ppm; [N_2] = balance; b = 10 °C min^{-1}; F = 1 SLM.

onset of gaseous N_2O at 130 °C, while the NH_3 TPD showed that NO was the primary gaseous oxidation product with an onset of 150 °C; correspondingly, DRIFTS analysis revealed adsorbed NH_3 oxidation products (*e.g.*, hyponitrite) upon contact at 150 °C (Fig. S7†). This indicates the gaseous product formed depends on the presence (TPR) or absence (TPD) of gas phase NH_3 and suggests that hyponitrite may be a common intermediate to the two pathways. The relatively low temperature oxidation of adsorbed NH_3 on $Ce_{0.7}Mn_{0.3}O_x$ suggests that the NO_2 evolved during NH_4NO_3 decomposition may have resulted from the global reaction shown in eqn (4). Here, the NO would originate from NH_4NO_3 dissociation to adsorbed NH_3 and nitric acid, followed by the autocatalytic oxidation of NH_3 to presumably adsorbed NO.

$$NO + NH_4NO_3 = N_2 + NO_2 + 2H_2O \quad (4)$$

We probed the reaction in eqn (4) *via* a temperature programmed surface reaction (TPSR) between adsorbed NH_4NO_3 and gas phase NO. As seen in Fig. 3b, the primary reaction product was NO_2 across the oxide and zeolite catalysts. The NO_2 that was evolved during the TPSR coincided with a depletion of the NO gas feed (Fig. S8†), which suggests the reaction represented by eqn (4) was the source of NO_2. Fig. 3b shows that the zeolite exhibited the expected one-to-one stoichiometry (from eqn (4)) between NO consumed and NO_2 evolved; in contrast, the quantity of NO consumed was half the NO_2 evolved on the oxide catalysts. The latter suggests that NH_4NO_3 thermal decomposition (*i.e.*, under N_2 purge, Fig. 3a) over the oxide catalysts proceeded at a rate comparable to the reaction rate of eqn (4). In other words, this suggests the thermal decomposition of NH_4NO_3 in N_2 occurred through the global reaction in eqn (4). This necessitates the oxidation of NH_3 by lattice oxygen, which is supported by NH_3 TPR (Fig. S7†).

Performing analogous TPSR experiments over the composite catalysts, *i.e.*, $Ce_xMn_{1-x}O_y$/H-SSZ-13, resulted in similar desorption profiles (Fig. S9†). In contrast to the bulk oxide materials, but in agreement with H-SSZ-13, the amount of NO consumed over the composite materials were in fair agreement with the amount of NO_2 evolved. The one-to-one stoichiometry suggests that most of the NH_4NO_3 resided on the zeolite after impregnation, as opposed to the oxide, and thereby minimized the autocatalytic decomposition of NH_4NO_3 during the TPSR. The diffusion of NH_4NO_3 from the zeolite to the oxide prior to its decomposition to NO_2 is implicit in the previous statement since the decomposition profile was oxide dependent (Fig. S9†). These data indicate that the oxide component, and in particular the Mn-containing oxide component, had a higher catalytic activity for the decomposition of NH_4NO_3 to NO_2 at intermediate temperatures (100–200 °C) relative to the zeolite. This temperature range coincides with the temperature range for SCR promotion by the mixed oxide in the composite system,[9] which suggests there may be relationship between NH_4NO_3 decomposition and SCR promotion.

The TPSR experiments indicate that the curvature change documented in Fig. 1b was caused by NH_4NO_3 decomposition *via* eqn (4). To explain, exposure of the $Ce_xMn_{1-x}O_y$/H-SSZ-13 catalysts to NH_3 prior to NO preferentially populated the zeolite with adsorbed ammonia. This is supported by the absent curvature change using the same protocol over the bulk $Ce_{0.7}Mn_{0.3}O_y$ oxide (Fig. S4†) and the much higher uptake of NH_3 on the zeolite compared to the bulk oxide (Fig. 4). As the temperature increased in Fig. 1b, NO oxidation to NO_2 (and its derivatives) occurred over the oxide and reacted with NH_3 from the zeolite to form NH_4NO_3, which subsequently reacted *via* eqn (4). However, given the non-steady-state nature of the experiment in Fig. 1b, the interplay between these two catalyst phases and the formation of NH_4NO_3 is less clear under actual SCR conditions. Nonetheless, these observations, and the prior observation that NH_3 storage (*i.e.*, Brønsted acidity) was required for the low-temperature SCR promotion by the mixed oxide,[9] provide a basis for understanding the synergy between the mixed oxide and zeolite components. In the absence of NH_3 storage sites, the oxide phase (*e.g.*, $Ce_{1-x}Mn_xO_y$) will catalyze the oxidation of NH_3 to NO_x at intermediate temperature, thereby restricting SCR performance (Fig. S7†). Thus, one apparent role of the zeolite phase in the $Ce_xMn_{1-x}O_y$/H-SSZ-13 composite system is to provide an adsorption site for NH_3 proximal to the oxide phase.

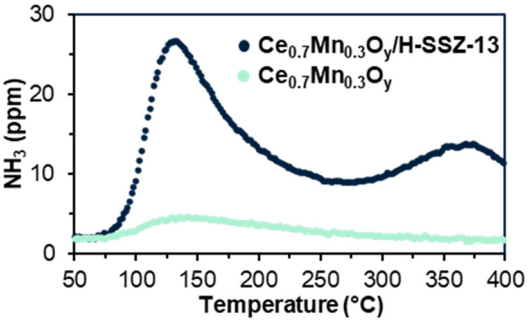

Fig. 4 NH_3 temperature programmed desorption (TPD) over bulk $Ce_{0.7}Mn_{0.3}O_y$ and $Ce_{0.7}Mn_{0.3}O_y$/SSZ-13. Both catalysts were heated to 500 °C in 15% O_2 for 0.5 h, followed by cooling under He, admittance of 350 ppm NH_3 for 0.5 h at 50 °C, and heating at 10 °C min^{-1} under 1 SLM N_2.

The mixed oxide component catalyzes NO oxidation to NO_2 (and derivatives) which, regardless of the underlying mechanism, allows access to fast SCR pathways under standard SCR gas feed. Table 1 summarizes possible SCR pathways that have been suggested by others.[15,16,20,21] Please note that these are known net gas phase reactions and not elementary steps occurring on a surface. The reaction network $N^{(1)}$ and $N^{(2)}$ represent standard SCR pathways; they differ in the way that nitrous acid (HNO_2) is formed which is regarded as the key intermediate leading to N_2 formation. For $N^{(1)}$ nitrous acid is formed through NO_2 disproportionation (R^2) and nitric acid reduction by NO (R^3). The latter reaction has been shown to occur under mild conditions;[20,22] indeed, the curvature change in Fig. 1b was caused by the higher rates of the reactions R^n that comprise NH_4NO_3 decomposition by NO, $N^{(3)}$, relative to NO oxidation, R^1. The former NO_2 disproportionation (R^2) reaction has also been shown to occur under mild conditions as it is a key step in NO_2 SCR, which is favored at low temperatures relative to standard and fast SCR.[13,23] This suggests that R^1 is a rate-controlling step for $N^{(1)}$ and implies that the rate of $N^{(1)}$ will tend to increase over materials with higher NO oxidation activity. This agrees with the general correlation between NO oxidation and low-temperature SCR activity observed here and elsewhere.[6,10]

Table 1 Possible reactions and pathways

		Reaction network			
Index	Net reaction	$N^{(1)}$	$N^{(2)}$	$N^{(3)}$	$N^{(4)}$
R^1	$2NO + O_2 = 2NO_2$	1	1	0	0
R^2	$2NO_2 + H_2O = HNO_2 + HNO_3$	2	0	0	1
R^3	$NO + HNO_3 = NO_2 + HNO_2$	2	0	1	0
R^4	$NH_3 + HNO_2 = N_2 + 2H_2O$	4	4	1	1
R^5	$NO + NO_2 = N_2O_3$	0	2	0	0
R^6	$N_2O_3 + H_2O = 2HNO_2$	0	2	0	0
R^7	$NH_4NO_3 = NH_3 + HNO_3$	0	0	1	-1
$N^{(1)}$	$4NO + O_2 + 4NH_3 = 4N_2 + 6H_2O$				
$N^{(2)}$	$4NO + O_2 + 4NH_3 = 4N_2 + 6H_2O$				
$N^{(3)}$	$NO + NH_4NO_3 = N_2 + NO_2 + H_2O$				
$N^{(4)}$	$2NH_3 + 2NO_2 = N_2 + NH_4NO_3 + H_2O$				

For reaction network $N^{(2)}$, nitrous acid is formed through the hydrolysis of dinitrogen trioxide (R^6). This reaction occurs readily at room temperature[24] and suggests that the rate limiting step for $N^{(2)}$ is either R^1 or R^5. Regardless of whether R^1 or R^5 is rate determining, the rate of $N^{(2)}$ will increase over materials with higher NO oxidation activity since the rate of R^5 is proportional to the concentration of NO_2. From the data obtained here it remains unclear whether $N^{(1)}$ or $N^{(2)}$ was kinetically dominate during standard SCR over the composite catalyst,[9] yet the kinetic relevance of NO oxidation (R^1) is manifested in both reaction networks. We hypothesize that the oxide phase in hybrid SCO–SCR systems catalyze the reactions that lead to nitrous acid formation and that these key intermediates react with NH_3 from and/or on the zeolite phase (R^4). In the absence of zeolite, R^4 is limited by the oxidation of NH_3 to NH_xO_y that occurred readily over $Ce_{0.7}Mn_{0.3}O_x$ (Fig. S7†).

Reaction network $N^{(3)}$ represents the NH_4NO_3 decomposition pathway that occurred over the $Ce_xMn_{1-x}O_y$ oxide phase in the presence and absence of gaseous NO (Fig. 3). The dissociation of NH_4NO_3 (R^7) is a prerequisite for $N^{(3)}$ to occur while the remaining reactions comprising $N^{(3)}$ (R^3 and R^4) occur below 100 °C. Thus, the dissociation reaction occurred readily over the ceria–manganese oxide phase relative to the zeolite phase, especially in the low temperature range (100–170 °C) (Fig. S6 and S7†). This may be a key contributing factor for the low temperature promotion observed in hybrid SCO–SCR systems. To be clear, fast and NO_2 SCR reactions that yield only N_2 and H_2O are limited below *ca.* 170 °C on zeolite materials due to NH_4NO_3 precipitation, $N^{(4)}$. The ability of ceria–manganese oxide to disfavor NH_4NO_3 formation (R^{-7}) prevents NH_3 competing with NO for free nitrate (R^3), and thereby, surface fast SCR reactions $N^{(1)}$ and $N^{(2)}$ can proceed at low temperature by circumventing reaction $N^{(4)}$.

Conclusions

It has been well-established that introducing a ceria–manganese mixed oxide to a zeolite provides access to low energy SCR pathways. We have identified a few possible contributing factors that may allow us to better understand the low energy pathways and rationalize the synergistic interaction between the mixed oxide and zeolite phase. Our data suggests that the oxide provides access to surface fast SCR channels through NO oxidation to adsorbed nitrogen dioxide and its derivatives. In the presence of nitrogen dioxide and ammonia, zeolites reversible deactivate from ammonium nitrate precipitation. However, ceria–manganese mixed oxides disfavor ammonium nitrate formation, and therefore, fast SCR reaction channels ostensibly remain accessible. We hypothesize that one primary role of the zeolite is to provide an ammonia reservoir for nitrogen dioxide (derivatives) to react with, since ammonia tends to oxidize on the surface of the mixed oxide. The unselective oxidation of these hybrid SCO–SCR materials remains a

primary technological hurdle to their industrial deployment for diesel application.

Conflicts of interest

There are no conflicts to declare.

Acknowledgements

The authors gratefully acknowledge the U.S. Department of Energy (DOE), Energy Efficiency and Renewable Energy (EERE), Vehicle Technologies Office for the financial support of this work. PNNL is operated for the DOE by Battelle under contract number DE-AC05-76RL01830.

Notes and references

1 K. Kamasamudram, N. W. Currier, X. Chen and A. Yezerets, *Catal. Today*, 2010, **151**, 212–222.
2 M. Koebel, M. Elsener and G. Madia, *Ind. Eng. Chem. Res.*, 2001, **40**, 52–59.
3 F. Gao, Y. Wang, M. Kollár, N. M. Washton, J. Szanyi and C. H. F. Peden, *Catal. Today*, 2015, **258**, 347–358; Y. Cui and F. Gao, *Emiss. Control Sci. Technol.*, 2019, **5**, 124–132.
4 A. Russell and W. S. Epling, *Catal. Rev.: Sci. Eng.*, 2011, **53**, 337–423.
5 T. Andana, K. G. Rappé, F. Gao, J. Szanyi, X. Pereira-Hernandez and Y. Wang, *Appl. Catal., B*, 2021, **291**, 120054.
6 M. Salazar, R. Becker and W. Grünert, *Appl. Catal., B*, 2015, **165**, 316–327.
7 A. I. Mytareva, A. Y. Stakheev, G. N. Baeva, D. A. Bokarev, A. L. Kustov and J. R. Thøgersen, *Top. Catal.*, 2016, **59**, 919–924.
8 M. Salazar, S. Hoffmann, O. P. Tkachenko, R. Becker and W. Grünert, *Appl. Catal., B*, 2016, **182**, 213–219; T. Liese, E. Löffler and W. Grünert, *J. Catal.*, 2001, **197**, 123–130.
9 T. Andana, K. G. Rappé, N. C. Nelson, F. Gao and Y. Wang, *Appl. Catal., B*, 2022, **316**, 121522.
10 A. Y. Stakheev, A. I. Mytareva, D. A. Bokarev, G. N. Baeva, D. S. Krivoruchenko, A. L. Kustov, M. Grill and J. R. Thøgersen, *Catal. Today*, 2015, **258**, 183–189.
11 A. A. Verma, S. A. Bates, T. Anggara, C. Paolucci, A. A. Parekh, K. Kamasamudram, A. Yezerets, J. T. Miller, W. N. Delgass, W. F. Schneider and F. H. Ribeiro, *J. Catal.*, 2014, **312**, 179–190; T. V. W. Janssens, H. Falsig, L. F. Lundegaard, P. N. R. Vennestrøm, S. B. Rasmussen, P. G. Moses, F. Giordanino, E. Borfecchia, K. A. Lomachenko, C. Lamberti, S. Bordiga, A. Godiksen, S. Mossin and P. Beato, *ACS Catal.*, 2015, **5**, 2832–2845; F. Gao, D. Mei, Y. Wang, J. Szanyi and C. H. F. Peden, *J. Am. Chem. Soc.*, 2017, **139**, 4935–4942.
12 C. Paolucci, A. A. Verma, S. A. Bates, V. F. Kispersky, J. T. Miller, R. Gounder, W. N. Delgass, F. H. Ribeiro and W. F. Schneider, *Angew. Chem., Int. Ed.*, 2014, **53**, 11828–11833; C. Paolucci, A. A. Parekh, I. Khurana, J. R. Di Iorio, H. Li, J. D. Albarracin Caballero, A. J. Shih, T. Anggara, W. N. Delgass, J. T. Miller, F. H. Ribeiro, R. Gounder and W. F. Schneider, *J. Am. Chem. Soc.*, 2016, **138**, 6028–6048.
13 M. Iwasaki and H. Shinjoh, *Appl. Catal., A*, 2010, **390**, 71–77.
14 H. Kubota, C. Liu, T. Toyao, Z. Maeno, M. Ogura, N. Nakazawa, S. Inagaki, Y. Kubota and K.-i. Shimizu, *ACS Catal.*, 2020, **10**, 2334–2344; C. Liu, G. Malta, H. Kubota, K. Kon, T. Toyao, Z. Maeno and K.-I. Shimizu, *J. Phys. Chem. C*, 2021, **125**, 13889–13899.
15 P. Forzatti, I. Nova and E. Tronconi, *Angew. Chem., Int. Ed.*, 2009, **48**, 8366–8368.
16 F. Marchitti, E. B. Hemings, I. Nova, P. Forzatti and E. Tronconi, *Emiss. Control Sci. Technol.*, 2016, **2**, 1–9.
17 G. Qi and W. Li, *Catal. Today*, 2015, **258**, 205–213.
18 M. Y. Mihaylov, E. Z. Ivanova, G. N. Vayssilov and K. I. Hadjiivanov, *Catal. Today*, 2020, **357**, 613–620.
19 M. Y. Mihaylov, E. Z. Ivanova, H. A. Aleksandrov, P. S. Petkov, G. N. Vayssilov and K. I. Hadjiivanov, *Mol. Catal.*, 2018, **451**, 114–124.
20 A. Grossale, I. Nova and E. Tronconi, *J. Catal.*, 2009, **265**, 141–147.
21 Q. Sun, Z.-X. Gao, H.-Y. Chen and W. M. H. Sachtler, *J. Catal.*, 2001, **201**, 89–99; A. Grossale, I. Nova, E. Tronconi, D. Chatterjee and M. Weibel, *J. Catal.*, 2008, **256**, 312–322.
22 A. Savara, M.-J. Li, W. M. H. Sachtler and E. Weitz, *Appl. Catal., B*, 2008, **81**, 251–257; Y. H. Yeom, J. Henao, M. J. Li, W. M. H. Sachtler and E. Weitz, *J. Catal.*, 2005, **231**, 181–193.
23 A. Grossale, I. Nova and E. Tronconi, *Catal. Lett.*, 2009, **130**, 525–531; I. Nova, C. Ciardelli, E. Tronconi, D. Chatterjee and B. Bandl-Konrad, *Catal. Today*, 2006, **114**, 3–12.
24 G. Y. Markovits, S. E. Schwartz and L. Newman, *Inorg. Chem.*, 1981, **20**, 445–450.

